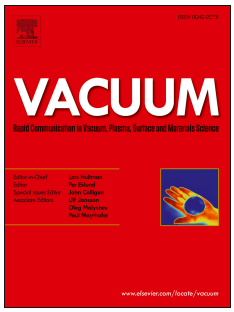

Epitaxial growth of oriented CoO films by radio-frequency sputtering deposition

In-Hui Hwang, Liliana Stan, Cheng-Jun Sun, Sang-Wook Han

PII: S0042-207X(23)00782-0

DOI: https://doi.org/10.1016/j.vacuum.2023.112585

Reference: VAC 112585

To appear in: *Vacuum*

Received Date: 15 May 2023

Revised Date: 18 August 2023

Accepted Date: 3 September 2023

Please cite this article as: Hwang I-H, Stan L, Sun C-J, Han S-W, Epitaxial growth of oriented CoO films by radio-frequency sputtering deposition, *Vacuum* (2023), doi: https://doi.org/10.1016/j.vacuum.2023.112585.

Epitaxial Growth of Oriented CoO Films by Radio-Frequency Sputtering Deposition

In-Hui Hwang[1], Liliana Stan[2], Cheng-Jun Sun[1], and Sang-Wook Han[3]*

[1]X-ray Science Division, Advanced Photon Source, Argonne National Laboratory, IL 60439, USA

[2]Center for Nanoscale Materials, Argonne National Laboratory, IL 60439, USA

[3]Department of Physics Education, Institute of Fusion Science, and Institute of Science Education, Jeonbuk National University, Jeonju 54896, Korea

*Correspondence and requests for materials should be addressed to S.-W.H. (shan@jbnu.ac.kr).

Abstract: Rock-salt CoO is a p-type semiconductor and its Néel temperature is close to room temperature. CoO-based compounds are known as promising systems for renewable energy harvest with high efficiency. CoO with catalytic and exchange bias properties can be widely used for industrial applications. In this paper, we report high-quality stable CoO(111) and (100) films epitaxially grown on *c*-cut (0001) and *r*-cut $(10\bar{1}2)$ α-Al_2O_3 substrates, respectively, using radio-frequency sputtering deposition. X-ray diffraction (XRD) measurements revealed that the CoO films had a rock-salt structure (*Fm3m*) with lattice constants of 4.2477 Å and 4.2617 Å for film grown on (0001) and $(10\bar{1}2)$ α-Al_2O_3 substrates, respectively. CoO films with the best crystal quality were grown at a substrate temperature of ~700 ºC. XRD measurements of CoO(111) films indicated a lack of structural residual strain, whereas CoO(100) films had substantial amounts of structural strain. X-ray reflectivity (XRR) and transmission electron microscopy measurements showed neither oxygen vacancy nor defects in both CoO(111) and (100) films. XRR revealed that the mean electron density of the CoO films was nearly identical to a pure CoO and that the films were considerably stable under the atmosphere.

Keywords: CoO, RF sputtering deposition, oxygen vacancy, epitaxial growth, thin film, surface roughness

1. Introduction

CoO is an attractive material for fundamental academic research as well as practical applications. CoO can form two different stable structures of rock-salt (*Fm3m*) and wurtzite (*P63mc*) space groups [1]. Bandgaps of rock-salt and wurtzite CoO are approximately 2.6 eV [2] and 1.6 eV [3], respectively. Rock-salt CoO is known as a direct transition p-type semiconductor. It is more stable than wurtzite CoO [4]. Rock-salt CoO is antiferromagnetic and paramagnetic below and above the Néel temperature of approximately 293 K, respectively [5,6]. The Néel temperature can be lowered to 225 K by reducing

the particle size of CoO [8] and raised up to 525 K by substituting Ni atom Co sites [7]. Prior studies have reported that CoO experiences an insulator-to-metal transition (MIT) at high pressures, which is accompanied by a magnetic collapse [6,9]. The antiferromagnetic phase of a rock-salt CoO is collapsed and the bandgap is closed at high pressures because an external pressure causes delocalization of 3*d* electrons of Co. The MIT of CoO, like other transition-metal oxides, such as NiO, MnO, and FeO [10] has been understood in terms of the Mott insulator, whereas it is somewhat different from that of VO_2, which is related to the alignment of V atoms at $T \geq T_c$ [11,12]. Co/CoO bilayers show the specific magnetic properties of exchange bias [13-16]. CoO layers with antiferromagnetic properties are known to play a key role in the exchange bias of magnetic layer/CoO systems, which can be used for the applications of memory devices [17-20].

Recently, several research groups have reported that CoO-based compounds could be promising materials as catalysts for renewable energy production [21-27]. Precious catalysts including Pt, Ru, and Rh have been widely used for practical applications to various systems. Since low cost, long-lived time, and stability of catalysts are essential for practical applications, transition-metal-based binary and ternary materials have been widely explored to replace precious catalysts [21]. Particularly, transition-metal oxides have attracted considerable attention for applications as photocatalysts because their catalysis can be activated by visible lights [28,29]. Jiang *et al*. have reported that CoO nanoparticles on nitrogen doped graphene hollow microspheres show the best performance in both oxygen reduction reaction (ORR) and oxygen evolution reaction (OER) [22]. Li-CoO-based materials have also been extensively studied for applications in rechargeable batteries [30-33], particularly air-metal batteries, because they are relatively safe and environmentally-friendly [34].

Although CoO has decent electrochemical properties and magnetic properties for practical applications, it is considerably difficult to synthesize high-quality CoO crystals with stable and reproducible properties because cobalt oxides can be easily formed into amorphous or Co_3O_4 [24]. Nanoparticles and meso-porous structures of CoO have been synthesized and characterized [8,22,27,34]. However, CoO is often mixed with Co_3O_4 because both CoO and Co_3O_4 have the same cubic structure with lattice constants of these two structures being quite similar to each other [2]. Various fabrication methods have been employed to synthesize CoO films, including pulsed-laser deposition [2], metal-organic-chemical-vapor deposition [24], chemical vapor deposition [35], and reactive sputtering deposition [36]. However, it is still a laborious task to synthesize single-phased CoO films with a uniform thickness and high quality. In this paper, we first report the synthesis of epitaxially-grown CoO(111) and (100) films with high-quality using radio-frequency (RF) sputtering deposition. We characterized the structural

properties, including oxygen vacancy, defects, and interfacial disorder, of CoO films using X-ray diffraction (XRD), glancing incidence X-ray reflectivity (XRR), and scanning transmission electron microscope (TEM) measurements.

2. Experimental details

CoO films were synthesized on *c*-cut (0001) and *r*-cut $(10\bar{1}2)$ α-Al_2O_3 substrates using a radio-frequency (RF) sputtering deposition system at the Center for Nanoscale Materials (CNM) of the Argonne National Laboratory. The base pressure of the growth chamber was kept below 10^{-8} Torr. After loading the substrates from the loading-lock chamber, to remove water and impurities, the substrates were heated and the temperature was maintained at 700 ℃ for ~30 minutes before starting the deposition of films. Argon gas with the purity of 99.999% with a flow rate of ~25 sccm was used and the pressure of the growth chamber was maintained at ~5 × 10^{-3} Torr during deposition. A 2 inch-diameter CoO target with a purity of 99.95 % was commercially obtained from Kurt J. Lesker and it was sputtered at an RF power of 125 W. The α-Al_2O_3(0001) and $(10\bar{1}2)$ substrates were placed side by side and simultaneously coated under the same growth conditions. The substrates with an area of 1 x 1 cm^2 were tightly held on a thick metal disk with a diameter of ~10 inch and a thickness of 0.5 inch to maintain a uniform temperature. We examined the CoO grown at various temperatures in the range of 400 ℃ – 780 ℃. The crystal properties of CoO films were characterized using XRD measurements with a tube X-ray source of Cu $K_{\alpha 1}$ radiation under the atmosphere. XRR measurements with the tube X-ray source under the atmosphere were performed to determine the mean thickness and surface roughness of CoO films. XRR can determine the mean electron density of a film, which provides information about the oxygen vacancy and the additional oxygen atoms existing at the CoO/Al_2O_3 interfaces as well as inside CoO films. The microstructural characterization of CoO films and CoO/Al_2O_3 interfaces were done using TEM measurements with a JEOL ARM 200CF model under the atmosphere. X-ray absorption near edge structure (XANES) measurements of CoO films were conducted at the Co K edge (7,709 eV) under the atmosphere to determine the chemical valence state of the Co ions in the CoO films. XANES measurements were performed at 20BM of Advanced Photon Source (APS) at Argonne National Laboratory and 8C of Pohang Light Source (PLS-II) at Pohang Accelerator Laboratory.

3. Results and Discussion

A crystal growth is a non-equilibrium phenomenon. Spatial gradient of temperature at the surface of growth is the most essential factor, although the growth of a crystalline film on a substrate is mainly

influenced by three parameters of substrate temperature, chamber pressure, and flow ratio of gases during deposition. A crystallization of a material on a substrate is considerably sensitive to the temperature of the substrate [37,38]. To determine the optimum growth conditions for CoO films with high quality, we deposited the CoO films at temperatures in the range of 400 – 780 ℃. Figure 1 shows the XRD by a low resolution (LRXRD) of CoO(111) films grown on *c*-cut α-Al_2O_3 substrates at different temperatures. No XRD peaks were observed from films grown at substrate temperatures below 400 ℃. This contrasts with previous reports on CoO films fabricated at room temperature using PLD and MOCVD [2,24], at 120 – 190 ℃ using CVD [35], and at ~100 ℃ using reactive sputtering deposition [36]. The inset of Fig. 1 shows XRD measurements with a high resolution (HRXRD) from CoO(111) films grown at different temperatures. The CoO(111) diffraction peak at $2\theta = 36.620^{\circ}$ at the substrate temperature of 400 ℃ corresponds to the lattice constant of 4.2469 Å. When the substrate temperature is increased from 400 ℃, the position of the CoO(111) peak moves slightly towards higher angles, indicating that the lattice constant of the CoO crystal decreases. The positions and the full width at half maximum of θ-2θ scans (FWHM-2θ) of XRD peaks are accurately determined by fitting the data using a Gaussian function. The peak positions and FWHM-2θ values of XRD from CoO(111) films grown at different substrate temperatures are listed in Table 1. As shown in the inset of Fig. 1, the intensity of the (111) peak increases and the FWHM-2θ decreases up to 700 ℃, denoting improvement in the crystal quality when the substrate temperature is increased up to 700 ℃. At a substrate temperature of 780 ℃, the (111) peak intensity decreases and the FWHM-2θ value increases implying a degradation of crystal quality. XRD results suggest that a CoO film with the best quality on Al_2O_3 substrates can be fabricated using a RF-sputtering deposition at a substrate temperature of approximately 700 ℃, much higher than the temperatures reported previously [2,24,35,36].

Figure 2 shows HRXRD data of CoO(111) films with different thicknesses. These films were grown at 700 ℃ for different durations of deposition of 10, 20, 30, and 60 minutes. The mean thickness of the CoO films determined using XRR measurements is proportional to the deposition duration. For a deposition duration of 60 minutes, the film thickness is approximately 112 nm. Exact thicknesses of these films are listed in Table 2. As shown in Fig. 2 (b), the CoO(111) peak position varies somewhat with the thickness, implying that the lattice constant depends on the thickness. HRXRD peaks are fitted with a Gaussian function to accurately determine peak positions and FWHM-2θ, as shown in Fig. 2 (b). Results of the best fits are listed in Table 2. The lattice constant of the CoO(111) with a thickness of ~17 nm is 4.2384 Å. It increases to 4.2641 Å for the film thickness of ~35 nm, then the lattice constant slightly decreases for thicker films. It is 4.2477 Å when the film thickness is ~112 nm. The lattice constants of the films are comparable to previous reports of 4.26 Å for the thickness of 13 nm [2]. The inset of Fig. 2 (a) shows FWHM-2θ as a function of film thickness. The FWHM-2θ is mainly affected

by the structural residual strain and thickness of a crystalline film [39]. The contribution of a crystalline film to the broadening of an XRD peak can be explained by the Scherrer equation as follows [40]:

$$\Delta\theta_L = \frac{K}{cos\theta}\left(\frac{\lambda}{L}\right), \quad (1)$$

where K is a dimensionless shape factor, λ is the wave length of incident X-rays, L is the film thickness, and θ is the Bragg angle. Assuming a structural residual stain (Δd) with a Gaussian distribution, the broadening of an XRD peak due to structural residual strain can be described as follows [41]:

$$\Delta\theta_R = tan\theta\left(\frac{\Delta d}{d}\right), \quad (2)$$

where d is the mean distance between atomic planes. Since the thickness and the residual strain of a crystal independently contribute to the broadening of an XRD peak, total broadening of an XRD peak can be obtained by summing squares of independent contributions with Eqs. (1) and (2) [39] as follows:

$$\Delta\theta = \sqrt{\frac{K^2}{cos^2\theta}\left(\frac{\lambda}{L}\right)^2 + tan^2\theta\left(\frac{\Delta d}{d}\right)^2}, \quad (3)$$

The relation between FWHM-2θ and the standard deviation of a Gaussian function is $\Delta\theta = \frac{FWHM-2\theta}{\sqrt{2ln2}}$. The solid line in the inset of Fig. 2 (a) is the best fit using Eq. (3). The best fit showed the shape factor $K = 0.73 \pm 0.02$ and residual strain $\Delta d_{CoO(111)} = 0.0073 \pm 0.0001$ Å. $K = 0.73$ is comparable to a good approximation value of 0.9 [40]. $\Delta d_{CoO(111)}$ is only ~0.3 % of $d = 2.4525$ Å. A small $\Delta d_{CoO(111)}$ indicates that structural strain in the CoO(111) films is negligible. This finding likely suggests a lack of residual strain in any directions of films because the (111) direction of rock-salt structured CoO is equally contributed by *x*-, *y*-, and *z*-directions. XRD measurements indicate a lack of structural defects, including oxygen vacancies and additional oxygen atoms in the CoO(111) films, independent of the film thickness. Figure 2 (c) shows θ-rocking curves of the CoO(111) diffraction of films with different thicknesses. The peak intensity and the FWHM of the θ-rocking curve (FWHM-θ) increase and decrease, respectively, as film thickness increases. θ-rocking curves are fitted well using a Gaussian function, as shown in Fig. 2 (c). A θ-rocking curve is mainly contributed by the mosaicity (direction distribution) and the thickness of crystals. FWHM-θs are nearly half the values of those of FWHM-2θ for the four films, as shown in the inset of Fig. 2 (a). This finding indicates that broadening of θ-rocking curves is also mainly influenced by film thickness and that the contribution of the mosaicity of films to the broadening is negligible. FWHM-θ values correspond well to the FWHM-2θ values of the films, strongly implying no structural defects due to grain boundaries on the films.

Figure 3 shows LRXRD results of CoO films grown on α-$Al_2O_3(10\bar{1}2)$ substrates. LRXRD measurements show only the (200) peak of a rock-salt CoO, indicating that the CoO films were grown

in the (100) direction on the substrates. Figure 3 (b) shows HRXRD patterns of CoO(100) peaks from films with various thicknesses. Peak positions remain at near the same angle. Meanwhile, the broadening of the peak varies with the film thickness. XRD peaks were fitted using a Gaussian function. Fit results are listed in Table 2. For a film with a thickness of ~109 nm, the CoO(100) diffraction peak is observed at 2θ = 42.385°, which corresponds to the lattice constant of a = 4.2617 Å. The lattice constant is somewhat larger than 4.2477 Å of CoO(111) film but is similar to those of previous reports [2,5]. The FWHM-2θ of the film with a thickness of ~18 nm is 1.27°, which is approximately 2.6 times larger than that of CoO(111) film with a thickness of ~17 nm. The FWHM-2θ value suddenly drops to below 0.6° for film thickness > 30 nm, as shown in the inset of Fig. 3 (a). The FWHM-2θ values of the CoO(100) films with different thicknesses were fitted with a single variable of Δd using Eq. (3) with K = 0.73. FWHM-2θ values of CoO(100) films are reasonably fitted except for a film with the thickness of ~18 nm. The best fit shows $\Delta d_{CoO(100)}$ = 0.043 ± 0.007 Å and a substantial amount of extra structural defects existing in the film with thickness of ~18 nm. The value of $\Delta d_{CoO(100)}$ is ~2% of the mean distance of the CoO (200) planes, indicating that CoO (100) films have a substantial amount of residual stain. Furthermore, the CoO film with a thickness of ~18 nm has a significant amount of extra strain, compared to that of thicker films. This result is greatly different from those of CoO(111) films, which show a lack of residual strain, as seen in Fig. 2. Figure 3 (c) shows θ-rocking curves of CoO(100) peaks. The mosaicity of CoO(100) films is considerably larger than that of CoO(111) films. For a thickness of ~109 nm, the FWHM-θ of the CoO(100) peak is ~4.76° which is approximately 100 times larger than ~0.046° of the CoO(111) peak with a thickness of ~112 nm. We could not obtain a satisfactory fit of the θ-rocking curves of CoO(100) films with a Gaussian function except for the film with a thickness of ~109 nm. The large mosaicity of CoO(100) films can be related to large values of FWHM-2θs that correspond to a disorder of interatomic distances. Due to lattice mismatch, CoO(100) crystals might barely form on the $Al_2O_3(10\bar{1}2)$ substrate at the initial growth stage. The FWHM-2θs and the FWHM-θs of the CoO(100) films indicate that the structural strain and the somewhat-random direction of the (100) crystals on the α-$Al_2O_3(10\bar{1}2)$ substrate gradually reduce when the film becomes thicker. The FWHM-θ and FWHM-2θ of the films suggest that there might be oxygen vacancies and/or additional oxygen atoms at the interface of the film/substrate and grain boundaries. XRD measures the only crystalline region of a specimen, meanwhile XRR can detect the microstructural properties of an entire specimen.

The mean interfacial structural properties and the mean electron density of the films were examined using XRR measurements. Figure 4 shows the XRR measurements of CoO films with different thicknesses. XRR is sensitive to thickness and interfacial structural properties as well as the electron density of films [39]. The interference of reflected X-rays from the surface of a film and the buried

interface of a film/substrate generates oscillations when XRR is measured as a function of the incident angle, as shown in Fig. 4. The period of the oscillations is inversely proportional to the film thickness. The critical angle of XRR is directly related to the mean electron density of a film, from which oxygen vacancies and additional oxygen atoms existing in a film can be estimated. To quantitatively determine the structural properties of the CoO films, XRR data were fitted to theoretical XRR with a Gaussian convolution of a surface roughness [39,42]. We obtained goodness fits of XRR data measured from CoO films, as shown in Fig. 4. The best fits showed that the mean electron density of the CoO films was ~0.4 % lower than ~1.827 electrons/Å^3 of a pure CoO crystal with a lattice constant of 4.2477 Å. The electron densities of the films were uniform. The difference in the electron density of the films from that of a pure CoO crystal is negligible, indicating a lack of oxygen vacancies and additional oxygen atoms in the films. This finding strongly suggests an absence of grain boundaries in the films, in which imperfect and/or amorphous phases exist. This corresponds to the XRD measurements which showed the CoO films having high crystalline quality. The thickness and the roughness of the films, which are determined by the best fits, are listed in Table 2. The thicknesses of both CoO(111) and (100) films are linearly proportional to the duration of the film deposition. The surface roughness (σ) of CoO(111) films is approximately 27 Å and nearly independent of the film thickness. The uniform surface roughness of CoO(111) films, independent of the thickness, strongly suggests that the films grew on an atomic scale in a step-by-step manner and that structural defects, including vacancy and structural strain, in the films are negligible. On the other hand, the σ of CoO(100) films for film thickness < ~460 Å is nearly half the σ value of CoO(111) films. When the thickness of CoO(100) films is larger than ~460 Å, the σ value suddenly increases. The XRD and XRR results suggest that a CoO(100) film grew in a fill-in way on α-$Al_2O_3(10\bar{1}2)$ substrate, overcoming a large lattice mismatch between the film and substrate. As a result, CoO(100) grains have a somewhat random orientation and the film surface becomes smooth at the initial stage of film growth. The crystals of CoO(100) film become more oriented and the structural strain reduces when the film is thicker.

Interfaces of both CoO(111)/Al_2O_3 and CoO(100)/Al_2O_3 are very clean with roughness less than 3 Å. The clean interfaces strongly suggest neither impurities nor water molecules existing on the substrate surface at the initial stage of the film growth. Although XRR cannot detect hydrogen atoms due to the limit of its sensitivity, the clean interfaces of both CoO(111) and (100) films on the substrates indicate a lack of hydrogen atom bonding at the interfaces. XRR results reveal that an extra layer with thickness of approximately 4 nm develops at the top of the (100) film with a thickness of ~38 nm. This extra layer increases to ~8 nm for the CoO(100) film with a thickness of ~109 nm. The electron density of the extra layer is approximately half of the electron density of a pure CoO. This is quite different from CoO(111) films on which no extra layers are observed. The extra layers existing near the surface of CoO(100)

films might be related to the surface roughness of films. Since XRR detects the mean density of films in the direction of thickness, it can perceive the region of a film, in which substantial amounts of structural defects and/or surface roughness exist, as a layer with a different electron density [39,43]. CoO(111) films with a high quality indicate that the influence of impurities such as water molecules in the growth chamber on CoO crystal growth is negligible. It is noted that the CoO(111) and (100) films were simultaneously deposited under the same growth conditions of base pressure of 10^{-8} Torr and substrate temperature of 700 ℃. The substantial amounts of structural defects in CoO(100) films can be ascribed to the lattice mismatch between the film and the substrate. Although XRR can measure the microstructural properties of an entire specimen, it can describe the only average properties of the specimen in the direction of film thickness. The microstructural details can be seen using TEM measurements.

Figure 5 (a) presents a scanning TEM (STEM) image of the CoO(111) film with a thickness of ~112 nm, that shows a clean interface of CoO(111)/Al_2O_3(0001) and some roughness on the film surface. Energy dispersive spectroscopy (EDS) measurements confirm uniformly-distributed O and Co atoms in the CoO film, as shown in Figs. 5 (b)-(c). The sharp interface of Co/substrate indicates a lack of interdiffusion of Co atoms at the interface. TEM measurements reveal two or three disordered atomic layers existing near the surface of the Al_2O_3 substrate and several disordered atomic layers of CoO developing at the interface, as shown in Fig. 5 (e). These disordered layers of the CoO(111) film at the interface are attributed to a lattice mismatch between CoO and Al_2O_3 and surface roughness of the substrate. Both planes of α-Al_2O_3(0001) and rock-salt CoO(111) have hexagonal shapes with lattice constants of Al_2O_3 a = 4.875 Å and CoO a = 4.2477 Å, respectively. Figures 5 (f) and (g) show TEM images of middle and top parts of the CoO film, in which neither structural disorder nor lattice distortion is visible. A lack of interatomic distance disorder at the surface of the CoO(111) film indicates that the CoO is quite stable under the atmosphere. Figure 5 (h) shows an image of small angle electron diffraction (SAED) from the CoO film. SAED shows neither extra phases nor amorphous parts existing in the measured region of the film. The TEM characterization results are in good agreement to XRD and XRR measurements.

Figure 6 shows the TEM images of CoO(100) film on the $Al_2O_3(10\bar{1}2)$ substrate. The STEM image indicates that the surface of the CoO(100) film is rougher than that of the CoO(111) film. The rough surface might correspond to the extra layer observed in XRR measurements, as discussed above. EDS analyses for O, Co, and Al elements reveal a lack of interdiffusion at the interface of the film and the substrate, as shown in Figs. 6 (b)-(d). Both TEM and SAED images suggest that the CoO film is

epitaxially grown in the (100) direction on the $Al_2O_3(10\bar{1}2)$ substrate. This corresponds well to XRD measurements. The TEM image near the interface of the CoO film and the substrate shows two or three disordered atomic layers developing on a smooth surface of the Al_2O_3 substrate due to lattice mismatch, as shown in Fig. 6 (e). The disordered atomic layer at the interface of CoO(100)/$Al_2O_3(10\bar{1}2)$ is smaller than that at the interface of CoO(111)/Al_2O_3(0001). The unit cell area of the $Al_2O_3[10\bar{1}2]$ plane is nearly twice that of the CoO [100] plane. A lattice mismatch between the two planes likely causes structural strain of CoO crystals on the substrate surface. The TEM image of the middle region of the CoO(100) film shows no visible structural disorder, while there are substantially-disordered atomic layers existing near the surface of the film, as shown in Figs. 6 (f) and (g). This might correspond to the rough surface of the film, as shown in the STEM image of Fig. 6 (a). These disordered atomic layers were likely developed when the film was exposed to the atmosphere because they were observed only near the surfaces, irrespective to film thickness. This suggests that the CoO(100) surface is less stable than the CoO(111) surface under the atmosphere. The SAED image further confirms neither structural disorder nor the second phase in the middle of the film. TEM results are somewhat different from XRD measurements which show a substantial amount of structural strain and a broad crystal orientation of the CoO(100) film. This disagreement is due to the facts that XRD measures the average crystalline structure of a large area, meanwhile TEM shows microstructural properties of a small region. The combination of XRD and TEM measurements for CoO(100) films suggest that a CoO(100) film is initially crystallized on $Al_2O_3(10\bar{1}2)$ in a pattern of small patches with slightly-different orientations. Subsequently, the film is gradually oriented in the (100) direction, when the film becomes thicker. A crystal growth in this manner has also been observed in ZnO nanorods on Al_2O_3 substrates [44].

The chemical properties of Co ions in the CoO films were examined using XANES measurements at the Co K edge, as shown in Fig. 7. The XANESs of both CoO(111) and (100) films were directly compared to those of a CoO powder, Co_3O_4 powder, and a Co foil. The main absorption edge of XANES is sensitive to the chemical valence state of the probing atoms. The main absorption edge of the films was 7,720 eV, which is identical to that of CoO powder. It is very different from the absorption edge of Co_3O_4, in which Co ions have the mixed chemical valence state of 2+ and 3+. The XANES measurements of the CoO films clarify that the chemical valence state of the Co ions in the films is mostly 2+, indicating a lack of extra phases and/or amorphous in the films. This corresponds well to the XRD, XRR, and TEM measurements. There is a slight variation in the absorption edge, in particular, of the CoO(111) films. It is well known that the XANES is contributed by the chemical valence state of a probing atom and the local structural properties of the nearest neighboring atoms [45,46]. XRD measurements of the CoO(111) films showed somewhat different lattice constants, as shown in Fig. 2 (b). The variation of the XANES signals of the CoO(111) films is ascribed to a slight difference in inter-

atomic distances rather than the chemical valence state of the Co ions in the films.

It is well known that each facet of a crystal has considerably different structural, chemical, and electrical properties with different behaviors in catalysis and sensitivity to gases [47-50]. Previous studies have demonstrated that the ORR of the CoO(111) surface is higher than that of the CoO(100) surface using density functional theory (DFT) calculations [51]. Other research groups have reported that the polar oxide (111) surface of CoO is thermodynamically unstable and strongly bonded with hydroxyls, and that termination Co ions of CoO(111) surfaces have a mixed chemical valence state of 3+ and 2+ [52-54]. Meyer *et al*. have suggested that a superstructure at the termination of CoO(111) surfaces might be due to the switch from a rock-salt phase to a wurtzite phase of CoO [55]. In the present study, TEM and XRR measurements reveal that both (111) and (100) surfaces of rock-salt CoO films are quite stable under the atmosphere, although some disordered layers develop near the surface of CoO(100) films. These stable surfaces of CoO(111) and (100) films suggest that their surfaces are likely to be terminated with oxygen atoms because an oxygen polar surface of transition metal oxides is known to be more stable than a metal polar surface [52,55,56]. This study implies that the crystallographical orientation of a CoO film can be controlled by selecting the proper facet of a substrate. The crystalline direction of a film is properly determined by the minimization process of surface energy during growth, reducing structural stress due to a lattice mismatch between a film and a substrate. Previous studies have also shown that crystal phases (rock-salt and wurtzite) of CoO could be selectively fabricated by controlling external parameters, including growth temperature and particle size [57-59]. When the size of a particle is small, CoO is likely to form a rock-salt structure. CoO will have a wurtzite structure with an increase in size. This study shows that CoO film keeps its initial structure phase as well as the crystalline direction, when the impurity level in the growth chamber is sufficiently low. Furthermore, once a CoO film forms with oxygen termination, the surface as well as the inside is considerably stable under the atmosphere. This study suggests that a CoO film in a specific crystalline direction with a large area and high quality can be fabricated on a proper substrate in a high vacuum chamber using RF-sputtering techniques.

4. Conclusions

This study shows that a CoO film in a specific crystalline direction with a large area and high quality can be fabricated on a proper substrate in a high vacuum chamber using RF-sputtering techniques. CoO(111) and (100) films with high quality were epitaxially-grown on α-Al_2O_3(0001) and $(10\bar{1}2)$ substrates, respectively, using RF-sputtering deposition at 700°C. XRD measurements showed a lack of structural residual strain in CoO(111) films, meanwhile CoO(100) films had a substantial amount of

strain. XRR measurements revealed that both CoO(111) and CoO(100) films were considerably stable under the atmosphere, although some disordered layers existed near the surfaces of CoO(100) films. TEM images further confirmed the highly crystalline order of both CoO(111) and (100) films in the middle of the films. XANES conformed that most of the Co ions in the CoO films had the chemical valence state of 2+, implying the absence of extra phases and/or amorphous phase in the films. This study showed that the epitaxially grown CoO film orientation can be tailored through the selection of the single-crystal substrate orientation in a high vacuum chamber. Epitaxially-grown CoO films with a high quality and a large area can be widely used as multifunctional materials, such as photocatalysts and electrode materials for water splitting.

Acknowledgement

The work was conducted under the auspices of the Basic Science Research Program through the National Research Foundation of Korea government grant funded by the Ministry of Science and ICT (No. 2020K1A3A7A09080403, No. 2021R111A3047300). CoO films were fabricated using a RF-sputtering system at the CNM of the Argonne National Laboratory. XANES measurements were performed at 20BM of APS at Argonne National Laboratory and at 8C of PLS-II at Pohang Accelerator Laboratory. Work performed at the Center for Nanoscale Materials and Advanced Photon Source, both U.S. Department of Energy Office of Science User Facilities, was supported by the U.S. DOE, Office of Basic Energy Sciences, under Contract No. DE-AC02-06CH11357.

References

[1] W.S. Seo, J.H. Shim, S.J. Oh, E.K. Lee, N.H. Hur, J.T. Park, Phase- and size-controlled synthesis of hexagonal and cubic CoO nanocrystals, J. Am. Chem. Soc. 127 (2005) 6188–6189, https://doi.org/10.1021/ja050359t.

[2] A. Matsuda, R. Yamauchi, D. Shiojiri, G. Tan, S. Kaneko, M. Yoshimoto, Room-temperature selective epitaxial growth of CoO(111) and Co_3O_4(111) thin films with atomic steps by pulsed laser deposition, Appl. Surf. Sci. 349 (2015) 78–82, https://doi:10.1016/j.apsusc.2015.04.205.

[3] Y. Wang, H.X. Ge, Y.P. Chen, X.Y. Meng, J. Ghanbaja, D. Horwat, J.F. Pierson, Wurtzite CoO: a direct band gap oxide suitable for a photovoltaic absorber, Chem. Commun. 54 **(**2018) 13949–13952, https://doi:10.1039/C8CC06777E.

[4] V.I. Anisimov, M.A. Korotin, E.Z. Kurmaev, Band-structure description of Mott insulators (NiO, MnO, FeO, CoO), J. Phys.: Condens. Matter. 2 (1990) 3973, https://doi:10.1088/0953-8984/2/17/008.

[5] M. Ghosh, E.V. Sampathkumaran, C.N.R. Rao, Synthesis and magnetic properties of CoO

nanoparticles, Chem. Mater. 17 (2005) 2348–2352, https://doi.org/10.1021/cm0478475.

[6] U.D. Wdowik, D. Legut. CoO under pressure from first principles, J. Phys. Chem. Solids 69 (2008) 1698–1703, https://doi.org/10.1016/j.jpcs.2007.12.014.

[7] V. A. Gavrichkov, Yu. S. Orlov, T. M. Ovchinnikova, S. G. Ovchinnikov, Mechanisms of the insulator—metal transition and spin crossover in CoO at high pressure, Jetp Lett. **112** (2020) 241–245, https://doi.org/10.1134/S0021364020160055.

[8] H. Shi, X. He, Large-scale synthesis and magnetic properties of cubic CoO nanoparticles, J. Phys. Chem. Solids 73, (2012) 646–650, https://doi.org/10.1016/j.jpcs.2012.01.001.

[9] A. Mandziak, G.D. Soria, J.E. Prieto, P. Prieto, C. Granados-Miralles, A. Quesada, M. Foerster, L. Aballe, J. de la Figuera, Tuning the Néel temperature in an antiferromagnet: the case of $Ni_xCo_{1-x}O$ microstructures, Sci. Rep. 9, (2019) 13584, (2019). https://doi.org/10.1038/s41598-019-49642-8.

[10] V. I. Anisimov, M. A. Korotin, E. Z. Kurmaev, Band-structure description of Mott insulators (NiO, MnO, FeO, CoO), J. Phys.: Condens. Matter 2 (1990) 3973, https://doi.org/10.1088/0953-8984/2/17/008

[11] I,-H. Hwang, C.-I. Park, S. Yeo, C.-J. Sun, S.-W. Han, Decoupling the metal insulator transition and crystal field effects of VO_2, Sci. Rep. 11 (2021) 3135, https://doi.org/10.1038/s41598-021-82588-4.

[12] I.-H. Hwang, Y. Park, J.-M. Choi, S.-W. Han, Direct comparison of the electrical, optical, and structural phase transitions of VO_2 on ZnO nanostructures, Current Appl. Phys. 36 (2022) 1, https://doi.org/10.1016/j.cap.2021.12.016.

[13] J. Demeter, E. Menendez, A. Teichert, R. Steitz, D. Paramanik, C. Van Haesendonck, A. Vantommea, K. Temst, Influence of magnetocrystalline anisotropy on the magnetization reversal mechanism in exchange bias Co/CoO bilayers, Solid State Commun. 152 (2012) 292–295, https://doi.org/10.1016/j.ssc.2011.11.026.

[14] J.A. Gonzalez, J.P. Andres, R.L. Anton, J.A. De Toro, P.S. Normile, P. Muniz, J.M. Riveiro, J. Nogues, Maximizing exchange bias in Co/CoO core/shell nanoparticles by lattice matching between the shell and the embedding matrix, Chem. Mater. 29 (2017) 5200–5206, https://doi.org/10.1021/acs.chemmater.7b00868.

[15] M. Öztürk, E. Sınır, E. Demirci, M. Erkovan, O. Öztürk, N. Akdoğan, Exchange bias properties of [Co/CoO]n multilayers, J. Appl. Phys. 112 (2012) 093911, https://doi.org/10.1063/1.4764107.

[16] L Smardz, U Köbler, W Zinn, Temperature and thickness dependence of unidirectional magnetic anisotropy effects in Co/CoO thin films, Vacuum 42 (1991) 283–285, https://doi.org/10.1016/0042-207X(91)90038-K.

[17] A. Saha, S. Sohoni, R. Viswanatha, Interface modeling leading to giant exchange bias from the $CoO/CoFe_2O_4$ quantum dot heterostructure, J. Phys. Chem. C 123 (2019) 2421−2427,

https://doi.org/10.1021/acs.jpcc.8b11124.

[18] L. Zhao, J. Xu, X. Shang, X. Li, Q. Li, S. Li, Synaptic memory devices from CoO/Nb:$SrTiO_3$ junction, R. Soc. Open Sci. 6 (2019), 181098, https://doi.org/10.1098/rsos.181098.

[19] T. Nozaki, S. Tamaru, M. Konoto, T. Nozaki, H. Kubota, A. Fukushima, S. Yuasa, Large voltage-induced coercivity change in Pt/Co/CoO/amorphous TiO_x structure and heavy metal insertion effect, Sci. Rep. 11 (2021) 21448, https://doi.org/10.1038/s41598-021-00960-w.

[20] R. Ai, W. Luo, X. Liu, Rectifier characteristics and analog bipolar resistive switching behavior in CoO-based memristor for artificial synapse application, Vacuum 188 (2021) 110190, https://doi.org/10.1016/j.vacuum.2021.110190.

[21] B. Zhang, X. Zheng, O. Voznyy, R. Comin, M. Bajdich, M. García-Melchor, L. Han, J. Xu, M. Liu, L. Zheng, F.P. García de Arquer, C.T. Dinh, F. Fan, M. Yuan, E. Yassitepe, N. Chen, T. Regier, P. Liu, Y. Li, P.D. Luna, A. Janmohamed, H.L. Xin, H. Yang, A. Vojvodic, E.H. Sargent, Homogeneously dispersed multimetal oxygen-evolving catalysts, Science 352 (2016) 333, DOI: 10.1126/science.aaf1525.

[22] Z.-J. Jiang, Z. Jiang, Interaction induced high catalytic activities of CoO nanoparticles grown on nitrogen-doped hollow graphene microspheres for oxygen reduction and evolution reactions, Sci. Rep. 6 (2016) 27081, https://doi.org/10.1038/srep27081.

[23] F.T. Haase, A. Bergmann, T.E. Jones, J. Timoshenko, A. Herzog, H.S. Jeon, C. Rettenmaier, B.R. Cuenya, Size effects and active state formation of cobalt oxide nanoparticles during the oxygen evolution reaction, Nat. Energy 7 (2022) 765–773, https://doi.org/10.1038/s41560-022-01083-w.

[24] J. Tyczkowski, R. Kapica, J. Łojewska, Thin cobalt oxide films for catalysis deposited by plasma-enhanced metal–organic chemical vapor deposition, Thin Solid Films 515 (2007) 6590–6595, https://doi.org/10.1016/j.tsf.2006.11.056.

[25] G. Dodekatos, J. Ternieden, S. Schünemann, C. Weidenthaler, H. Tüysüz, Promoting effect of solvent on Cu/CoO catalyst for selective glycerol oxidation under alkaline conditions, Catal. Sci. Technol. 8 (2018) 4891–4899, https://doi.org/10.1039/C8CY01284A.

[26] J. Jin, K. Walczak, M.R. Singh, C. Karp, N.S. Lewis, C. Xiang, Energy Environ. Sci. 7 (2014) 3371 – 3380, https://doi.org/10.1039/C4EE01824A.

[27] A. Lu, Y. Chen, J. Jin, G.-H. Yue, D.-L. Peng, CoO nanocrystals as a highly active catalyst for the generation of hydrogen from hydrolysis of sodium borohydride, J. Power Sources 220 (2012) 391–398, https://doi.org/10.1016/j.jpowsour.2012.08.010.

[28] R. Marschall, L. Wang, Non-metal doping of transition metal oxides for visible-light photocatalysis, Catalysis Today 225 (2014) 111–135, https://doi.org/10.1016/j.cattod.2013.10.088.

[29] J.-S. Jeon, B.-H. Kim, C.-I. Park, S.-Y. Seo, C. Kwak, S.-H. Kim, S.-W. Han, In-situ X-ray

absorption fine structure study of TiO_2 nanoparticles under ultraviolet light, Jpn. J. Appl. Phys. 49 (2010) 031105, https://doi.org/10.1143/JJAP.49.031105.

[30] C. Shang, S. Dong, P. Hu, J. Guan, D. Xiao, X. Chen, L. Zhang, L. Gu, G. Cui, L. Chen, Compatible interface design of CoO-based Li-O_2 battery cathodes with long-cycling stability, Sci. Rep. 5 (2015) 8335, https://doi.org/10.1038/srep08335.

[31] A.K. Rai, L.T. Anh, J. Gim, J. Kim, One-step synthesis of CoO anode material for rechargeable lithium-ion batteries, Ceram. Int. 39 (2013) 9325–9330, https://doi.org/10.1016/j.ceramint.2013.05.049.

[32] J. Wang, J. Zheng, X. Liu, The key to improving the performance of Li–air batteries: recent progress and challenges of the catalysts, Phys. Chem. Chem. Phys. 24 (2022) 17920–17940, https://doi.org/10.1039/D2CP02212E.

[33] Q. Zhou, H. Xu, L. lv, W. Liu, Y. Liang, H. Li, T. Chen, Study on the decline mechanism of cathode material LiCoO2 for Li-ion battery, Vacuum 177 (2020) 109313, https://doi.org/10.1016/j.vacuum.2020.109313.

[34] Q. Dai, J. Tang, The optical and magnetic properties of CoO and Co nanocrystals prepared by a facile technique, Nanoscale 5 (2013) 7512–7519, https://doi.org/10.1039/C3NR01971C.

[35] E. Amin-Chalhoub, T. Duguet, D. Samelor, O. Debieu, E. Ungureanu, C. Vahlas, Chemical vapor deposition of low reflective cobalt (II) oxide films, Appl. Surf. Sci. 360 (2016) 540–546, https://doi.org/10.1016/j.apsusc.2015.10.188.

[36] M.J. Carey, F.E. Spada, A.E. Berkowitz, W. Cao, G. Thomas, Preparation and structural characterization of sputtered CoO, NiO, and $Ni_{0.5}Co_{0.5}O$ thin epitaxial films, J. Mater. Research 6 (1991) 2680–2687, https://doi.org/10.1557/JMR.1991.2680.

[37] Z. Jin, C. Park, S.-W. Han, B. Jiang, Selective synthesis and structural stability of anatase and rutile $Ti_{1-x}Fe_xO_2$ nanoparticles, J. Korean Phys. Soc. 61 (2012) 222–226, https://doi.org/10.3938/jkps.61.222.

[38] W. Li, G. Yu, S. Wang, J. Ding, X. Xu, Q. Gu, D. Wang, P. Huang, Influence of temperature on the growth and surface morphology of Fe3+ poisoned KDP crystals, RSC Adv. 7 (2017) 17531 – 17538, https://doi.org/10.1039/C6RA25710K.

[39] S.-W. Han, S. Tripathy, P. F. Miceli, M. Covington, L. H. Greene, M. Aprili, X-Ray reflectivity study of interdiffusion at $YBa_2Cu_3O_{7-x}$ and metal interfaces, Jpn. J. Appl. Phys. 42 (2003) 1395, https://doi:10.1143/JJAP.42.1395.

[40] U. Holzwarth, N. Gibson, The Scherrer equation versus the Debye-Scherrer equation, Nature Nanotech 6 (2011) 534, https://doi.org/10.1038/nnano.2011.145.

[41] B.E. Warren, X-ray Diffraction (1990) pp. 72, Dover Publication, INC., New York.

[42] S.K. Sinha, E.B. Sirota, S. Garoff, H.B. Stanley, X-ray and neutron scattering from rough surfaces,

Phys. Rev. B 38 (1988) 2297, https://doi.org/10.1103/PhysRevB.38.2297.

[43] S.-W. Han, J.A. Pitney, P.F. Miceli, M. Covington, L.H. Greene, M.J. Godbole, D.H. Lowndes, X-ray reflectivity study of thin film oxide superconductors, Physica B 221 (1996) 235–237, https://doi.org/10.1016/0921-4526(95)00931-0.

[44] C. Kwak, B.-H. Kim, C.-I. Park, S.-H. Park, S.-Y. Seo, S.-H. Kim, S.-W. Han, Microstructural properties at the interfaces of ZnO nanorods and ZnO homo-buffer layers, J. Nanosci. Nanotechnol. 10 (2010) 912-918, https://doi.org/10.1166/jnn.2010.1895.

[45] J. J. Rehr and R. C. Albers, Theoretical approaches to x-ray absorption fine structure, Rev. Mod. Phys. 72 (2000) 621–654, https://doi.org/10.1103/RevModPhys.72.621.

[46] S.-W. Han, Fundamentals of XAFS (2016) Baleon.

[47] M. Núñez, J.L. Lansford, D.G. Vlachos, Optimization of the facet structure of transition-metal catalysts applied to the oxygen reduction reaction, Nat. Chem. 11 (2019) 449, https://doi.org/10.1038/s41557-019-0247-4.

[48] B. Song, S. Si, A. Soleymani, Y. Xin, H.E. Hagelin-Weaver, Effect of ceria surface facet on stability and reactivity of isolated platinum atoms, Nano Res. 15 (2022) 5922–5932, https://doi.org/10.1007/s12274-022-4251-4.

[49] X. Gao, T. Zhang, An overview: Facet-dependent metal oxide semiconductor gas sensors, Sensors and Actuators B: Chemical 277 (2018) 604–633, https://doi.org/10.1016/j.snb.2018.08.129.

[50] A. Hermawan, A.T. Hanindriyo, K. Hongo, R. Maezono, S. Yin, Impact of surface faceting on gas sensing selectivity of NiO: revealing the adsorption sites of organic vapors on the {111} facet, J. Phys. Chem. C 126 (2022) 8037–8046, https://doi.org/10.1021/acs.jpcc.2c00092.

[51] B. Qin, Y. Tian, P. Zhang, Z. Yang, G. Zhang, Z. Cai, Y. Li, A density functional theory study of the oxygen reduction reaction on the (111) and (100) surfaces of cobalt(II) oxide, Prog. React. Kinet. and Mech.44 (2019) 122–131, https://doi.org/10.1177/1468678319825727.

[52] D. Cappus, M. Haβel, E. Neuhaus, M. Heber, F. Rohr, H.-J. Freund, Polar surfaces of oxides: reactivity and reconstruction, Surf. Sci. 337 (1995) 268–277, https://doi.org/10.1016/0039-6028(95)00624-9.

[53] J. Forsythe, O. Leiko, V. Uvarov, J. Škvára, J. Mysliveček, K. Mašek, V. Johánek, CoO epitaxial growth on Cu(111) by reactive PVD and plasma oxidation, Surface Interfaces 34 (2022) 102364, https://doi.org/10.1016/j.surfin.2022.102364.

[54] S.P. Chenakin, N. Kruse, Surface compositional changes upon heating cobalt oxalate dihydrate in vacuum, Vacuum 187 (2021) 110090, https://doi.org/10.1016/j.vacuum.2021.110090.

[55] W. Meyer, K. Biedermann, M. Gubo, L. Hammer, K. Heinz, Superstructure in the termination of

CoO(111) surfaces: Low-energy electron diffraction and scanning tunneling microscopy, Phys. Rev. B 79 (2009) 121403(R), https://doi.org/10.1103/PhysRevB.79.121403.

[56] S.-W. Han, H.-J. Yoo, Sung Jin An, Jinkyoung Yoo, Gyu-Chul Yi, Orientation-dependent x-ray absorption fine structure of ZnO nanorods, Appl. Phys. Lett. 86 (2005) 021917, https://doi.org/10.1063/1.1851616.

[57] K.M. Nam, J.H. Shim, D.-W. Han, H.S. Kwon, Y.-M. Kang, Y. Li, H. Song, W.S. Seo, J.T. Park, Syntheses and characterization of wurtzite CoO, rocksalt CoO, and spinel Co_3O_4 nanocrystals: their interconversion and tuning of phase and morphology, Chem. Mater. 22 (2010) 4446–4454, https://doi.org/10.1021/cm101138h.

[58] K.Y. Jang, S.J. Ahn, J.-H. Kwon, K.M. Nam, Y.H. Kim, Novel route from a wurtzite to a rock-salt structure in CoO nanocrystals: in situ transmission electron microscopy study, J. Phys. Chem. C 123 (2019) 10689–10694, https://doi.org/10.1021/acs.jpcc.9b01548.

[59] I.V. Golosovsky, M. Estrader, A. López-Ortega, A.G. Roca, L. López-Conesa, E. Del Corro, S. Estradé, F. Peiró, I. Puente-Orench, J. Nogués, Zinc blende and wurtzite CoO polymorph nanoparticles: Rational synthesis and commensurate and incommensurate magnetic order, Appl. Mater. Today 16 (2019) 322–331, https://doi.org/10.1016/j.apmt.2019.06.005.

Temperature	400°C	500°C	600°C	700°C	780°C
2θ(°) of CoO(111)	36.620 ± 0.001	36.508 ± 0.001	36.518 ± 0.001	36.582 ± 0.001	36.682 ± 0.001
FWHM-2θ(°)-	0.359 ± 0.003	0.173 ± 0.002	0.158 ± 0.002	0.153 ± 0.001	0.173 ± 0.002

Table 1. Peak positions (2θ) and FWHM-2θs of HRXRD from CoO(111) films grown at different temperatures.

Growth duration	10 min	20 min	30 min	60 min
2θ(°) of CoO(111)	36.696 ± 0.001	36.467 ± 0.001	36.471 ± 0.001	36.613 ± 0.002
FWHM-2θ (°)	0.487 ± 0.004	0.237 ± 0.002	0.170 ± 0.003	0.0943 ± 0.0004
a (Å)	4.2384 ± 0.0001	4.2641 ± 0.0001	4.2637 ± 0.0001	4.2477 ± 0.0002
Thickness (Å)	165.4 ± 0.5	352.3 ± 0.5	514.0 ± 1.0	1120.0 ± 4.0
Roughness σ (Å)	28.33 ± 0.05	26.52 ± 0.05	26.00 ± 0.05	27.90 ± 0.02
Growth duration	10 min	20 min	30 min	60 min
2θ(°) of CoO(200)	42.384 ± 0.011	42.395 ± 0.017	42.434 ± 0.013	42.385 ± 0.005
FWHM-2θ (°)	1.265 ± 0.031	0.600 ± 0.047	0.553 ± 0.035	0.459 ± 0.013
a (Å)	4.2618 ± 0.0014	4.2607 ± 0.0021	4.2570 ± 0.0016	4.2617 ± 0.0006
Thickness (Å)	182.7 ± 0.1	380.4 ± 0.5	465.4 ± 1.3	1093.3 ± 2.6
Roughness σ (Å)	12.75 ± 0.07	12.1 ± 0.1	28.2 ± 0.3	24.7 ± 0.2

Table 2. Structural properties of (top) CoO(111) and (bottom) CoO(100) films determined using HRXRD and XRR measurements. HRXRD peak positions (2θ) and FWHM-2θs of CoO(111) and (200) diffractions are shown; Thickness and surface roughness (σ) of films were determined using XRR as discussed in the text.

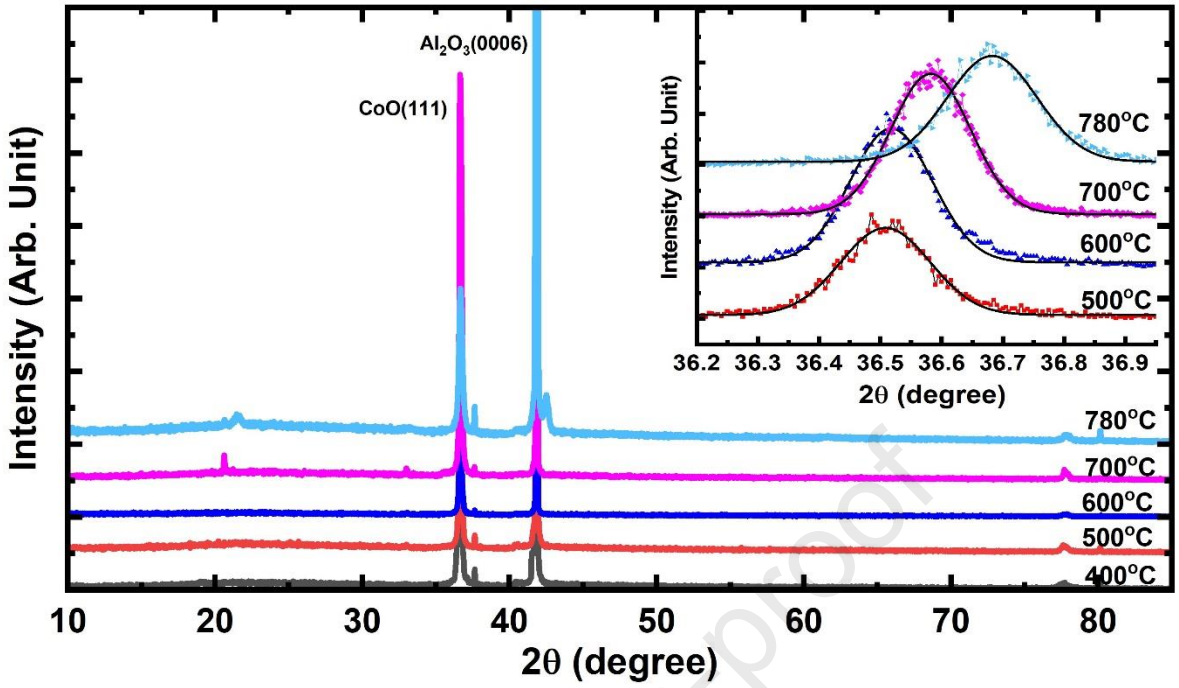

Figure 1. LRXRD from CoO(111) films on α-Al_2O_3(0001) substrates grown at different temperatures. The inset shows HRXRD of CoO(111) peaks. Black-solid lines are the best fits with a Gaussian function.

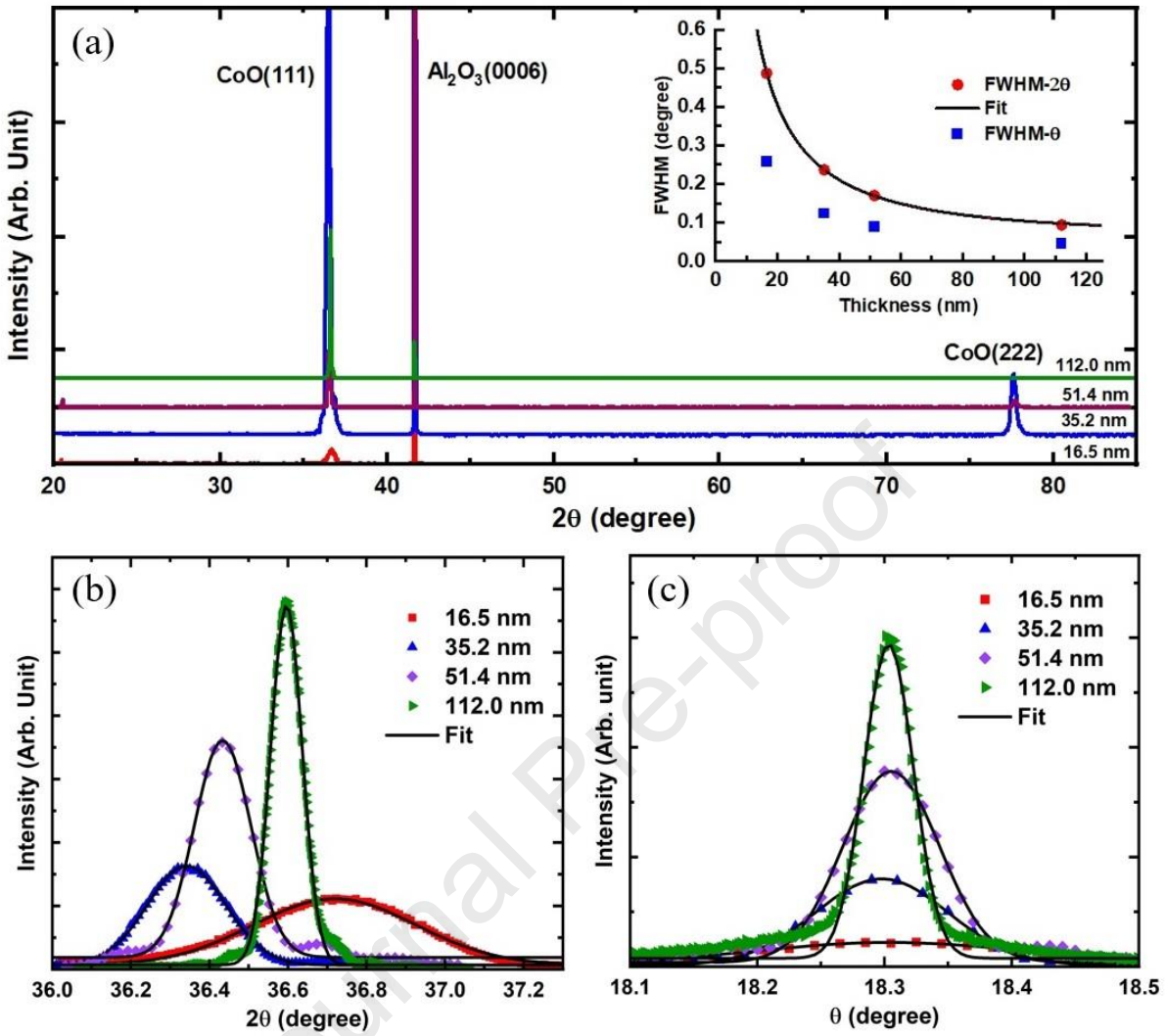

Figure 2. (a) HRXRD from CoO(111) films with different thicknesses grown on α-Al_2O_3(0001) substrates. The data was vertically shifted for clarity. (b) Horizontal expansion near the CoO(111) peak of the HRXRD. (c) θ-rocking curves of CoO(111) diffractions. Solid lines in (b) and (c) are the best fits using a Gaussian function. Red dots and blue squares in the inset of (a) show FWHMs of θ-2θ scans and θ-rocking curves of CoO(111) diffractions shown in (b) and (c), respectively, as a function of film thickness. The solid line in the inset of (a) is the best fit using Eq. (3).

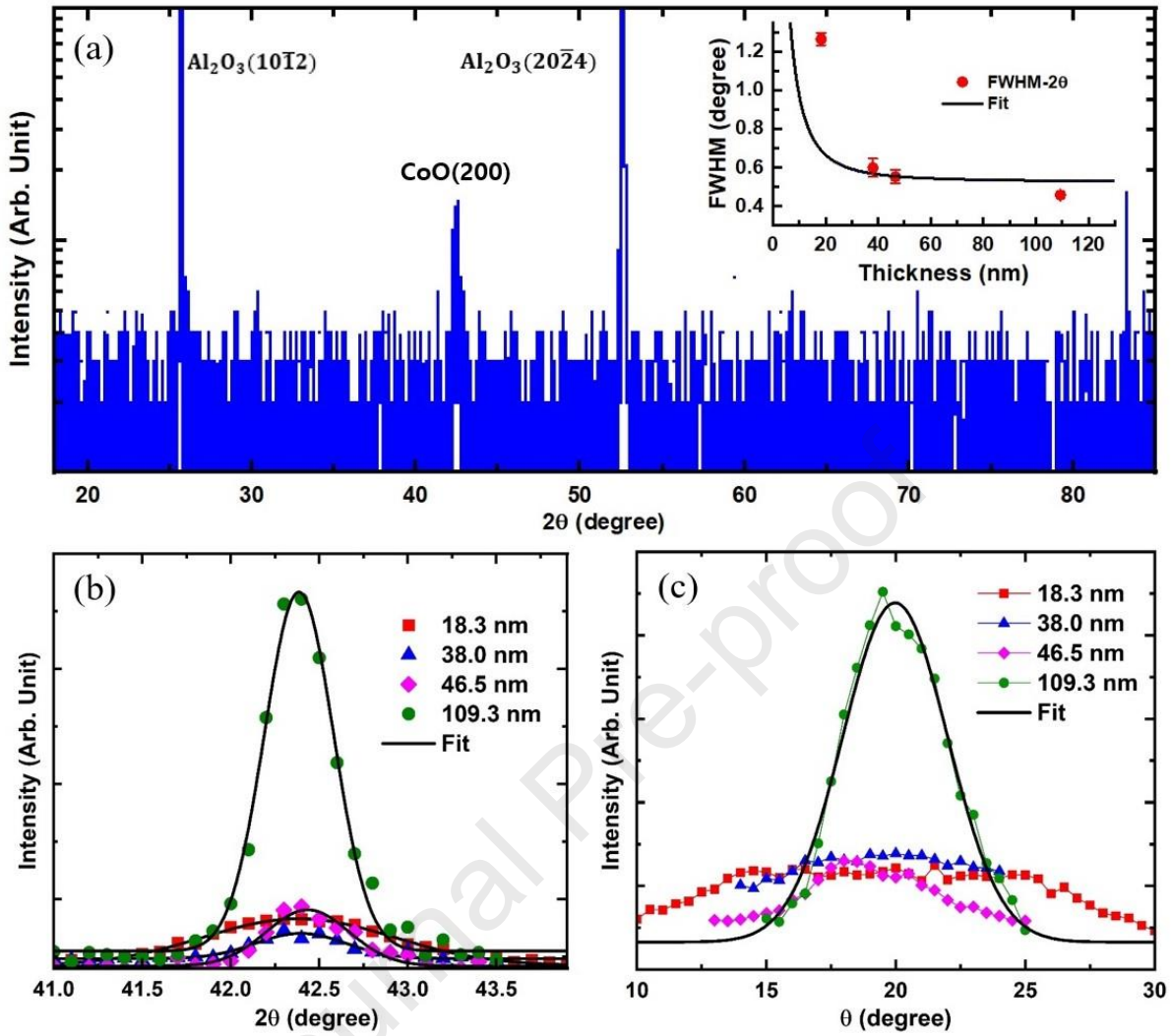

Figure 3. (a) LRXRD from CoO (100) films with a thickness of 109.3 nm on the α-Al_2O_3($\mathbf{10\bar{1}2}$) substrate. (b) and (c) θ-2θ scans and θ-rocking curves, respectively, of the CoO (200) peak of films with different thicknesses. Solid lines in (b) and (c) are the best fits with a Gaussian function. Inset of (a) shows FWHM-2θs of CoO (200) diffractions in (b) as a function of film thickness. Solid line is the best fit using Eq. (3).

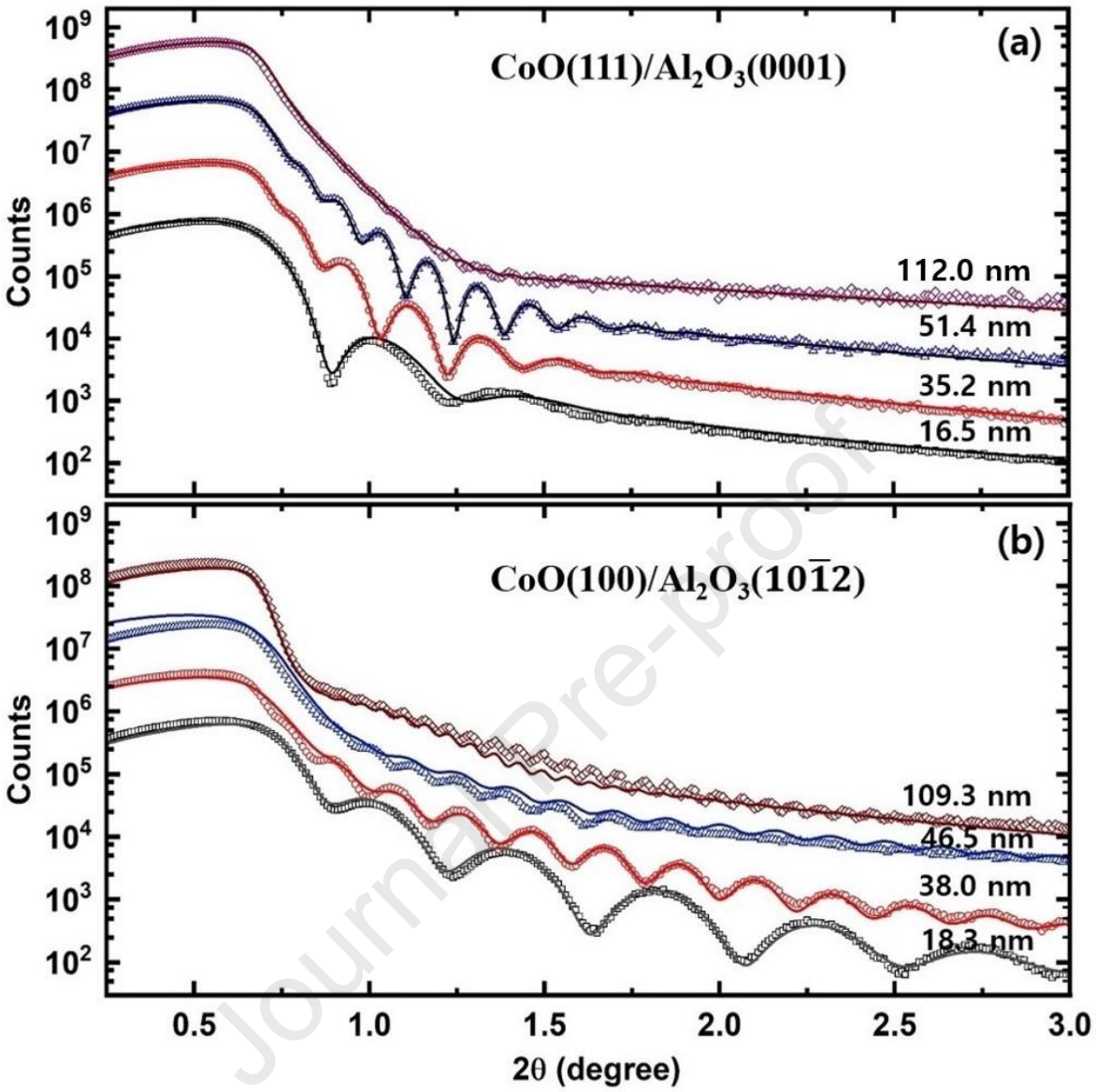

Figure 4. XRR from (a) CoO(111)/Al_2O_3(0001) and (b) CoO(100)/Al_2O_3($\mathbf{10\bar{1}2}$) with different thicknesses of the CoO film as a function of 2θ. Data is vertically shifted for clarity. Open symbols and solid lines are measured data and the best fits, respectively.

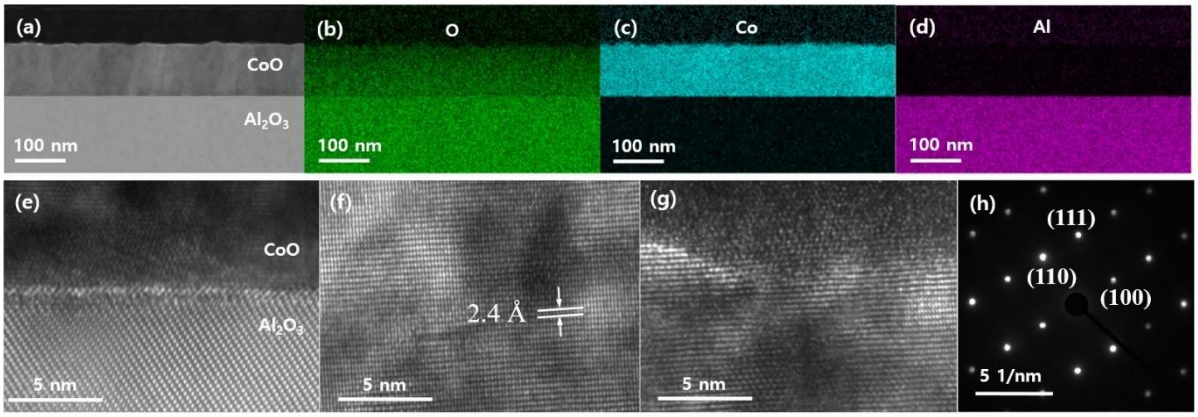

Figure 5. (a) STEM and EDS images of (b) O, (c) Co, and (d) Al distributions from CoO(111) film with a thickness of 81.9 nm. (e), (f), and (g) are TEM images of CoO(111)/α-Al_2O_3(0001), near the interface, in the middle, and near the surface of the film, respectively. (h) SAED is of middle part of the film.

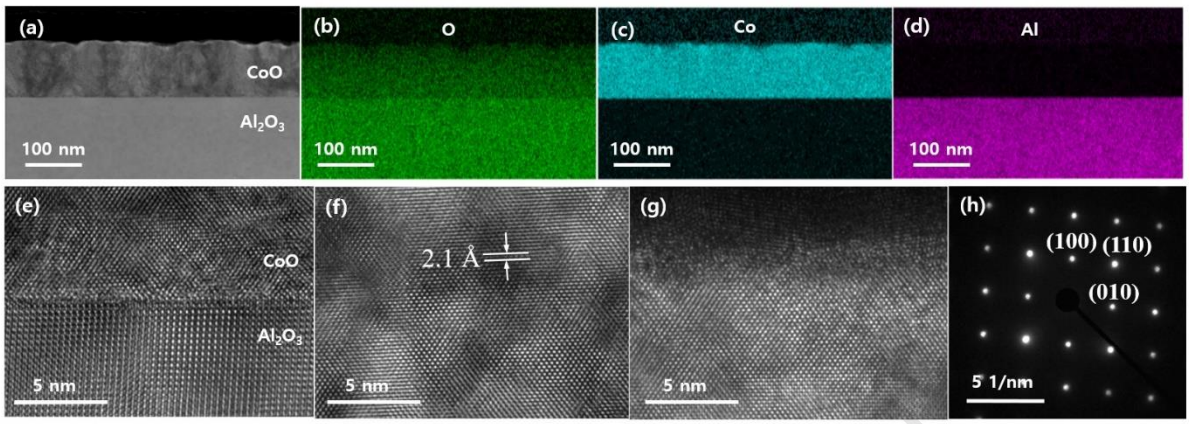

Figure 6. (a) STEM and EDS images of (b) O, (c) Co, and (d) Al from CoO(100) film with a thickness of 109.3 nm. (e), (f), and (g) are TEM images of CoO(100)/α-Al_2O_3($\mathbf{10\bar{1}2}$), near the interface, in the middle, and near the surface of the CoO film, respectively. (h) SAED is of the middle of the film.

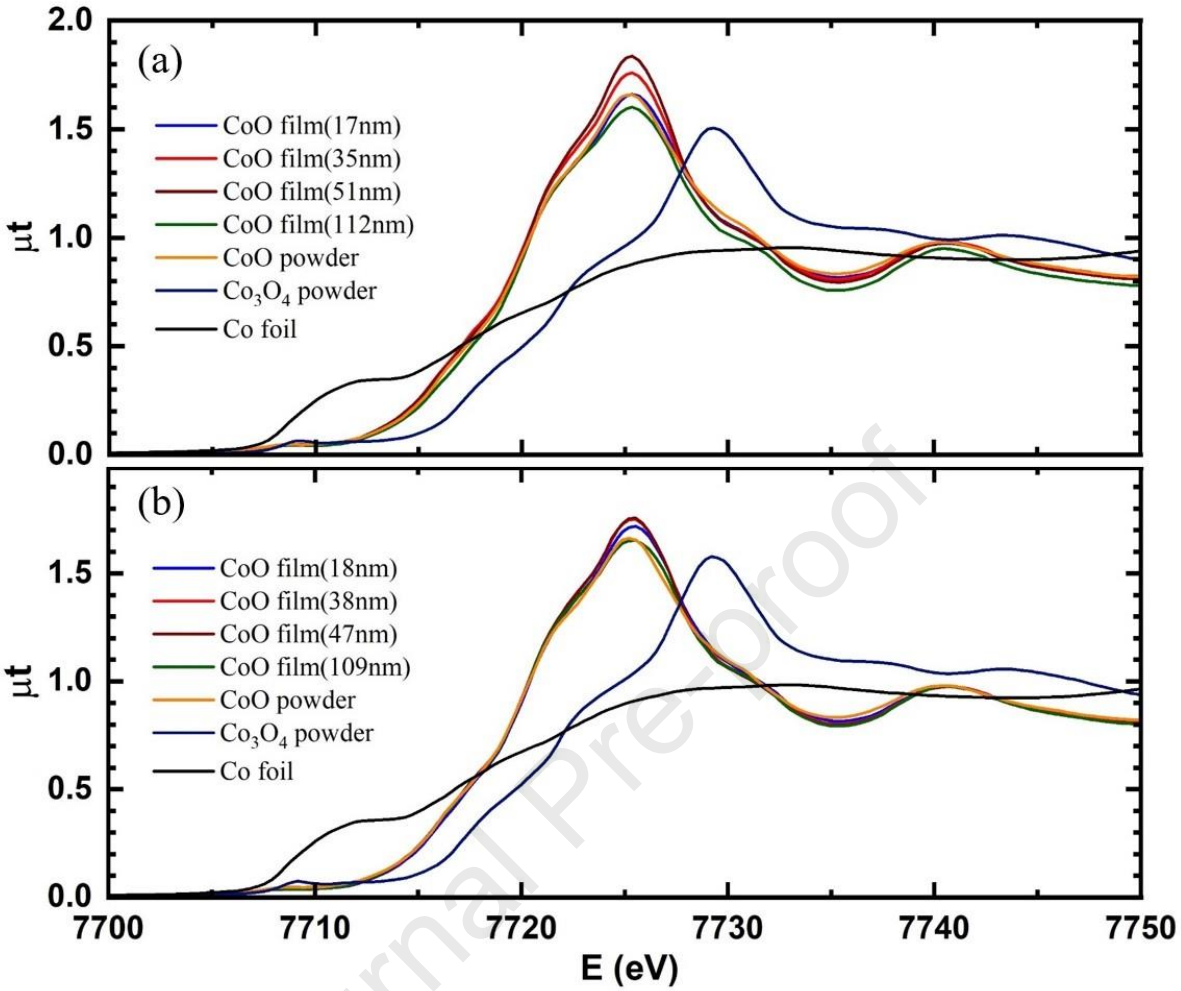

Figure 7. Normalized total X-ray absorption (μt) from (a) CoO(111) films and (b) CoO(100) films with different thicknesses, and CoO powder, Co_3O_4 powder, and Co foil at the Co K edge as a function of the incident X-ray energy.

Highlights

- (111)- and (100)-oriented CoO films are epitaxially synthesized in a high vacuum chamber using RF-sputtering techniques.
- The crystallinity and structural properties of the films are quantitatively analyzed using X-ray diffraction, X-ray reflectivity, and TEM measurements.
- The films are considerably stable under the atmosphere.
- High quality CoO films in a specific crystalline direction with a large area can be fabricated in a high vacuum chamber using RF-sputtering techniques.

Declaration of interests

☒ The authors declare that they have no known competing financial interests or personal relationships that could have appeared to influence the work reported in this paper.

☐The authors declare the following financial interests/personal relationships which may be considered as potential competing interests: